

Supporting Online Material

Incised Valley Fill Description (IVF) and Eustatic Justification. The fall and rise in sea level that is recorded by the IVF complex at Wadi Al-Hitan occurs within the base of Calcareous Nannoplankton Zone NP19-20 (Fig. DR1) and cannot, therefore, represent more than several 10^5 years. It nevertheless is important to consider the possibility that vertical crustal motion was an important contributor to local relative sea level change (Watts, 1982; Moucha et al., 2008). Sediments from tectonically active regions commonly record numerous episodes of exposure and submergence as a result of crustal deformation, which can easily overwhelm any signal from global eustatic sea level change (Cisne, 1986). However, there is little evidence for tectonic activity in the WH region that would have resulted in the rapid ($<10^6$ years), large-magnitude (10's of meters), uplift followed immediately by subsidence of comparable magnitude that would be required to form the marine sediment-encased IVF. Indeed, such oscillatory patterns (uplift followed subsidence) of crustal deformation on timescales less than 10^6 years rarely occur.

Nevertheless, long-duration crustal flexure and deformation has significantly affected patterns of sedimentation at WH. For example, the overall thickness of the late Eocene section at WH is controlled by sea level and long-term thermal subsidence and crustal downwarping that occurred on timescales of $\geq 10^6$ years (Moucha et al., 2008). Important regional tectonic compression and regional reactivation of normal faults as reverse faults also began in the Bartonian (~ 39 Ma), during the collision of the African/Arabian Plate and the Eurasian Plate (Guiraud and Bosworth, 1999). However, this regional compressive event manifested most strongly east of Cairo, in the Sinai Peninsula region, and caused sustained, long-term crustal flexure and uplift. Ultimately, this and later deformation related to the opening of the Red Sea caused broad uplift of the region and the erosion and exposure of the E-O boundary sections at WH. Thus, the weight of geologic evidence suggests that tectonic factors have conspired to make determination of absolute sea level in the late Eocene (measured relative to today's sea level datum) difficult or impossible, but that tectonics has not strongly affected our ability to estimate the relative magnitudes of the shorter-term sea level rises and falls that were required to form the IVF complex.

Additional support for the hypothesis that global eustatic sea level change was responsible for the IVF complex at WH comes from sequence stratigraphic analyses conducted in other geographic regions. Previous work (Peters et al., 2009) and the biostratigraphic data presented here (Fig. DR1) indicate that the sequence boundary at the base of the IVF is equivalent to the Pr-2 sequence boundary that has been identified in Europe and elsewhere (Hardenbol et al., 1998). Thus, evidence for a significant sequence boundary caused by sea level fall and rise near the base of NP19-20 is not limited to Egypt.

Isostatic adjustment and gravitational geoid. IVF incision depth is controlled principally by sea level fall, which is affected by both eustatic sea level change and local uplift and subsidence (Wellner et al., 2007). We address possible regional isostatic effects of the removal of 10-20 m of ocean water prior to river incision following techniques similar to those used on Lake Bonneville shorelines (Crittenden, 1960). Specifically, we assume that ocean water depresses the crust by ~25% of its depth. Thus, removing 10 m of ocean water results in ~2.5 m of isostatic rebound and 20 m of ocean water results in ~5 m of isostatic rebound. This rebound would increase the magnitude of the effective base level fall and, therefore, the resultant depth of the IVF. Thus, we subtract the regional isostatic effect from the measured IVF depth in order to more precisely estimate the strictly eustatic component.

Redistribution of mass on the Earth's surface, such as that which occurs during ice sheet growth, affects the gravitational geoid and, therefore, absolute sea surface elevation (Clark et al, 2002; Mitrovika et al., 2009). Precisely estimating the regionally variable, but potentially large, gravitational geoid effect is more difficult because no simulations have yet been conducted where Antarctica is glaciated to ~70% of its present volume and where paleogeography is restored to late Eocene configurations. However, because model calculations for the retreat of the present-day Antarctic Ice Sheet suggest a low sensitivity for the eastern Mediterranean region (i.e., ~1.05 times greater than the eustatic change; Clark et al., 2002; Mitrovika et al., 2009; Bamber et al., 2009). Thus, perturbation to the geoid is unlikely to be the principal control on base level fall at WH and, therefore, IVF depth. Nevertheless, we include this effect in our

estimate of eustatic sea level change so as to provide a conservative minimum estimate, noting that the actual amount of sea level fall is likely to have been somewhat larger (~1-2 m) than our estimate.

Calculating ocean $\delta^{18}\text{O}$ and temperature change. We convert the estimated eustatic sea level change to ocean $\delta^{18}\text{O}$ by first dividing the IVF-constrained sea level change by the surface area of the ocean during the late Eocene (adjusting for the modestly larger ocean surface area in the late Eocene does not significantly affect our results). We then assume an Antarctic ice $\delta^{18}\text{O}$ of $-30 \pm 5 \text{‰}$ (DeConto et al., 2008) and calculate the change in mean ocean $\delta^{18}\text{O}$ from the average pre-excursion $\delta^{18}\text{O}$ amount of 1.6‰ , weighting by the total mass volume of ocean water when there is no continental ice ($1.39 \times 10^9 \text{ km}^3$) relative to the total mass volume of ice growth ($1.48 \pm 0.07 \times 10^7 \text{ km}^3$). This result depends on significantly on the $\delta^{18}\text{O}$ value of Antarctic ice. Our estimate is based on the climate model simulations of DeConto et al. (2008), who suggested an average Antarctic $\delta^{18}\text{O}$ of -30 to -35‰ for the full Oligocene ice sheet. During the growth phase of ice, however, the value is lower -20 to -25‰ . We thus assume the mean and error $-30 \pm 5 \text{‰}$. We would note that other arguments for lower Antarctic $\delta^{18}\text{O}$ of -45‰ (e.g., Katz et al., 2008) required the growth of ice to 20 % larger than present volumes (i.e., ice caps existing in Labrador or Scandinavia) at the E-O Boundary, a result in conflict with both climate model simulations (DeConto et al., 2008; Lunt et al., 2008) and paleo-records that suggest only potential transient valley glacier presence on Greenland during the E-O (Eldrett et al., 2007) and the development of an ice cap during the Miocene (Larsen et al., 1994). The agreement between our predicted ocean $\delta^{18}\text{O}$ change and the observed $\sim 0.30 \text{‰}$ $\delta^{18}\text{O}$ increase supports our use of the higher Antarctic ice $\delta^{18}\text{O}$.

Maximum eustatic sea level fall and $\delta^{18}\text{O}$ change. To provide a conservative minimum estimate of the glacioeustatic sea level fall, we have chosen to ignore the fact that some amount of seawater had to be removed from the area prior to fluvial incision. This additional drop in sea level, which is evidenced by the transition from marine to non-marine environments during IVF formation, could be included in our estimate, but it is difficult to precisely constrain the actual absolute depth of the shallow marine environment on the basis of sedimentological and fossil data. Nevertheless, adding 10 m to our estimate,

which is a reasonable upper limit for deposition of the sediments that underlie the IVF (see Supplemental Figures), increases the total eustatic estimate to -50 ± 2 m. A sea level fall of this magnitude represents an ice volume equivalent that is close to the present-day volume of the East Antarctic Ice Sheet. Assuming an isotopic composition of Antarctic ice of -30 ± 5 ‰, this sea level equivalent volume of ice growth would change ocean $\delta^{18}\text{O}$ by $+0.41 \pm 0.08$ ‰, which is slightly larger than the $+0.30$ ‰ excursion that is observed in the globally averaged $\delta^{18}\text{O}$ stack but still overlapping when considering the error in $\delta^{18}\text{O}$ stack (Zachos et al., 2001, 2008).

Timing of ocean $\delta^{18}\text{O}$ and $^{87}\text{Sr}/^{86}\text{Sr}$, and CO_2 changes. The $\delta^{18}\text{O}$ stack of Zachos *et al.* (2001, 2008) is a compilation of multiple benthic $\delta^{18}\text{O}$ records that have been correlated on the basis of magnetic polarity and biostratigraphic zones, the latter of which permits correlation with the marine sediments that enclose the IVF at WH. The most direct comparison is from ODP site 689B in the Southern Ocean (Kennett et al., 1990). Site 689B has the highest resolution benthic $\delta^{18}\text{O}$ for this time period in the Zachos *et al.* (1990) stack and it also has $^{87}\text{Sr}/^{86}\text{Sr}$ measurements (Mead and Hodell, 1995). At site 689B, the ~ 0.30 ‰ increase in $\delta^{18}\text{O}$ and the $\sim 4.2 \times 10^{-5}$ increase in $^{87}\text{Sr}/^{86}\text{Sr}$ occur within polarity chron C16 (Kennett et al., 1990; Mead and Hodell, 1995), which brackets the interval from upper NP18 to lower NP19-20 (Gradstein et al., 2004). This age is consistent with the lower Zone NP19-20 assignment of the IVF, as indicated by the co-occurrence of the calcareous nannofossils *Isthmolithus recurvus* and *Neococcolithes minutus* (Fig. DR1) within the enclosing marine sediments (Martini, 1971; Perch-Nielsen, 1989).

The CO_2 record of Pagani *et al.* (2005) for the late Eocene to Oligocene is from DSDP site 612. The decrease in CO_2 that we note occurred in calcareous nannoplankton Zone CP15b, the base of which is equivalent to the NP18/NP19-20 boundary (Gradstein et al., 2004). Thus, given the limits of the correlation tools that can be applied to these multiple independent records, it is impossible to reject the hypothesis that the sea level fall recorded by the IVF at WH, the positive $\delta^{18}\text{O}$ excursion observed at site 689B and in the global average $\delta^{18}\text{O}$ stack, the $^{87}\text{Sr}/^{86}\text{Sr}$ increase, and the drop in CO_2 are all

approximately coeval. Given the internal consistency of these independent observations, the most parsimonious explanation is that they are all related to a transient, large-scale glaciation of Antarctica at ~36.0 Ma.

The following figures and their captions provide a more complete geological picture of the Wadi Al-Hitan study area than can be presented in the manuscript. The figures also provide more complete documentation of the evidence that was used to constrain the timing, genesis, and magnitude of the sea level fall and rise that formed the incised valley fill (IVF) complex and its subsidiary sequence boundaries.

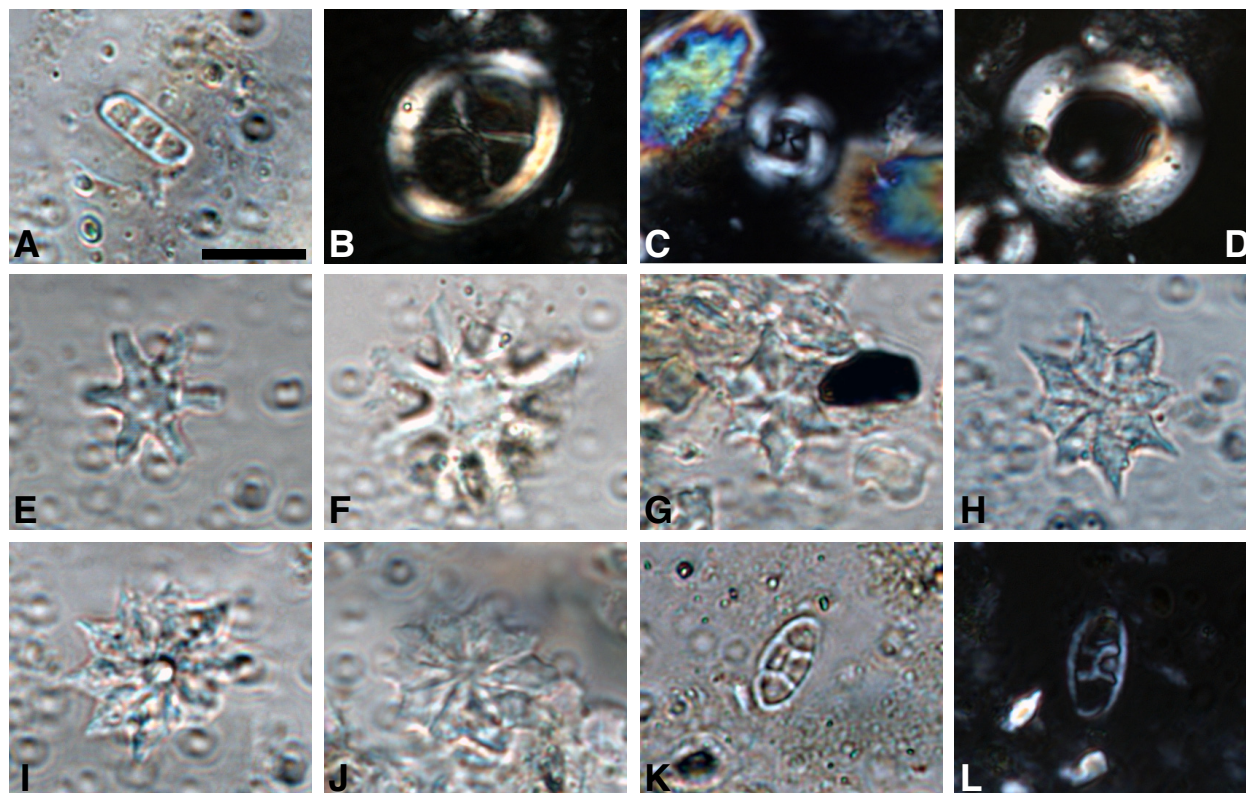


Figure DR1. Photomicrographs of diagnostic calcareous nannoplankton from marine sediments enclosing the IVF at WH. PL plain light, CP, crossed polars. (A) *Isthmolithus recurvus* Deflandre, PL. (B) *Chiasmolithus oamarunensis* (Deflandre), CP. (C) *Reticulofenestra reticulata* (Gartner and Smith), CP. (D) *Reticulofenestra umbilica* (Levin), CP. (E) *Discoaster tanii* Bramlette, PL. (F) *Discoaster cf. tanii nodifer* Bramlette, PL. (G-H) *Discoaster saipanensis* Martini, PL. (I-J) *Discoaster barbadiensis* Bramlette and Riedel, PL. (K-L) *Neococcolithes minutus* (Perch-Nielsen). Calcareous nannofossils are most abundant in deeper shelf sediments below the sequence boundary, but well-preserved specimens of all of these taxa have been found in marine sediments above the sequence boundary, which is ~100 m below the E-O boundary at WH (Fig. DR10). This assemblage is diagnostic of lower NP19-20 and, barring a dominant contribution of fossils from sediment reworking, suggests that the IVF formed within the first few hundred thousand years after the first appearance of *Isthmolithus recurvus* at ~36 Ma (Hardenbol et al., 1998; Gradstein et al., 2004). All images taken at the same magnification, scale bar ~ 5 μ m.

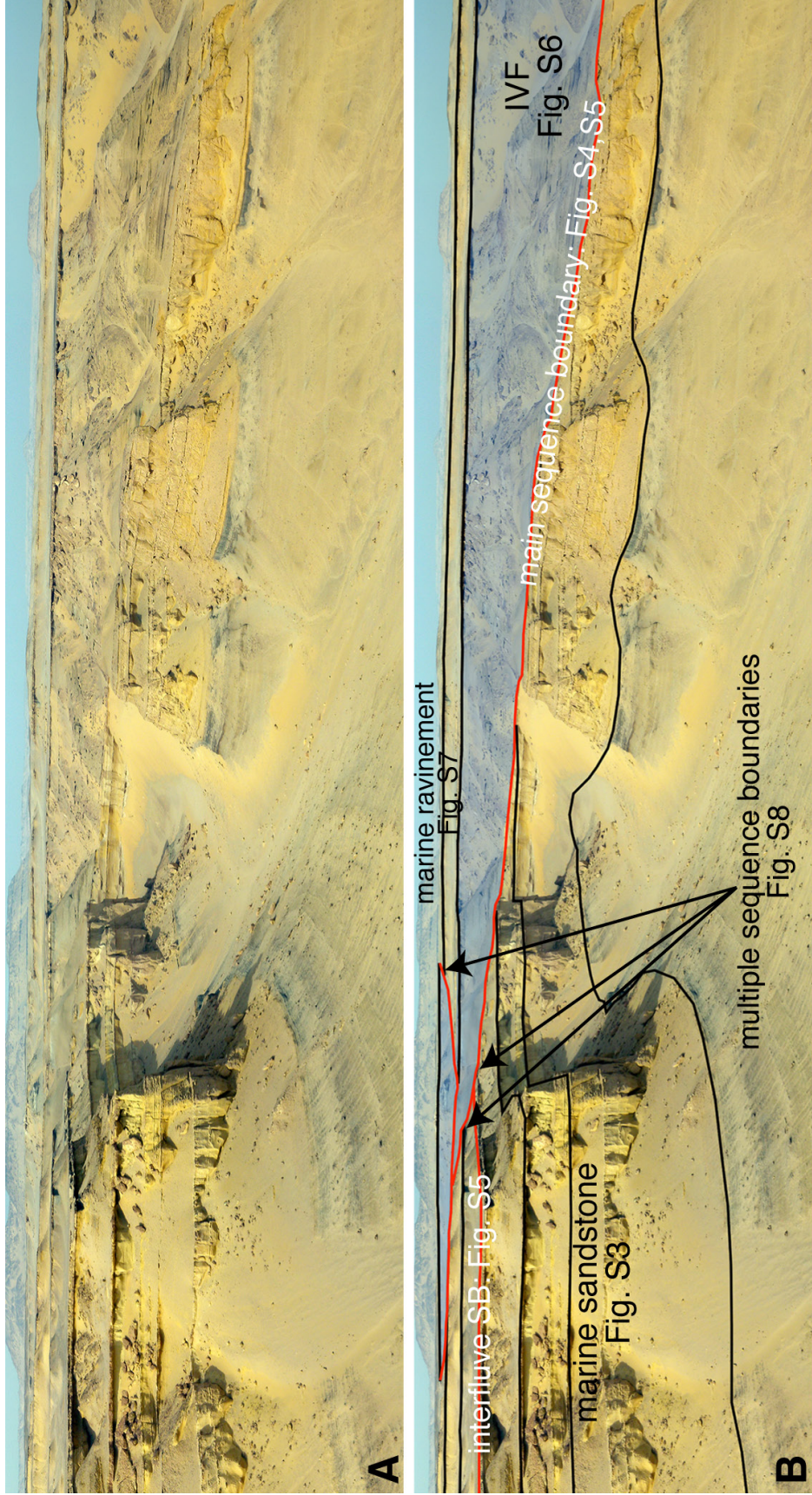


Figure DR2. Panorama overview images of the lateral (southern) margin of the IVF and its adjacent interfluvial. It is unusual to have such a completely exposed IVF complex and, therefore, unambiguous constraints on IVF geometry and the nature of the transition with overlying marine shelf sediments. (A) Raw image with no annotation. Compare to B. (B) Image from A with key features identified, along with position of underlying yellowish marine sandstone and the nature of the upper IVF contact. In particular, note the termination of the well-defined ledges that consist of marine skeletal shell beds (arrows in B) into the body of the IVF. These truncations represent separate sequence boundaries that record the drowning and flooding of the region and the formation of a compound IVF.



Figure DR3. Very fine sandstone immediately underlying the IVF at WH. (A) *Ophiomorpha* in cross sectional view. (B) *Ophiomorpha* in plan view. (C) Vertical cross section exposure through very fine sandstone showing numerous *Ophiomorpha* and other clay- and pellet-lined vertical burrows. (D) internal moulds of turritellid gastropods, with smaller fragments of ostreiid oysters. The body and trace fossils within these very fine sandstones, which immediately underlie the IVF, indicate deposition in the soft, sandy-bottomed environments of the middle to upper shoreface, within intertidal to shallow subtidal zone (MacEachern et al., 2007).

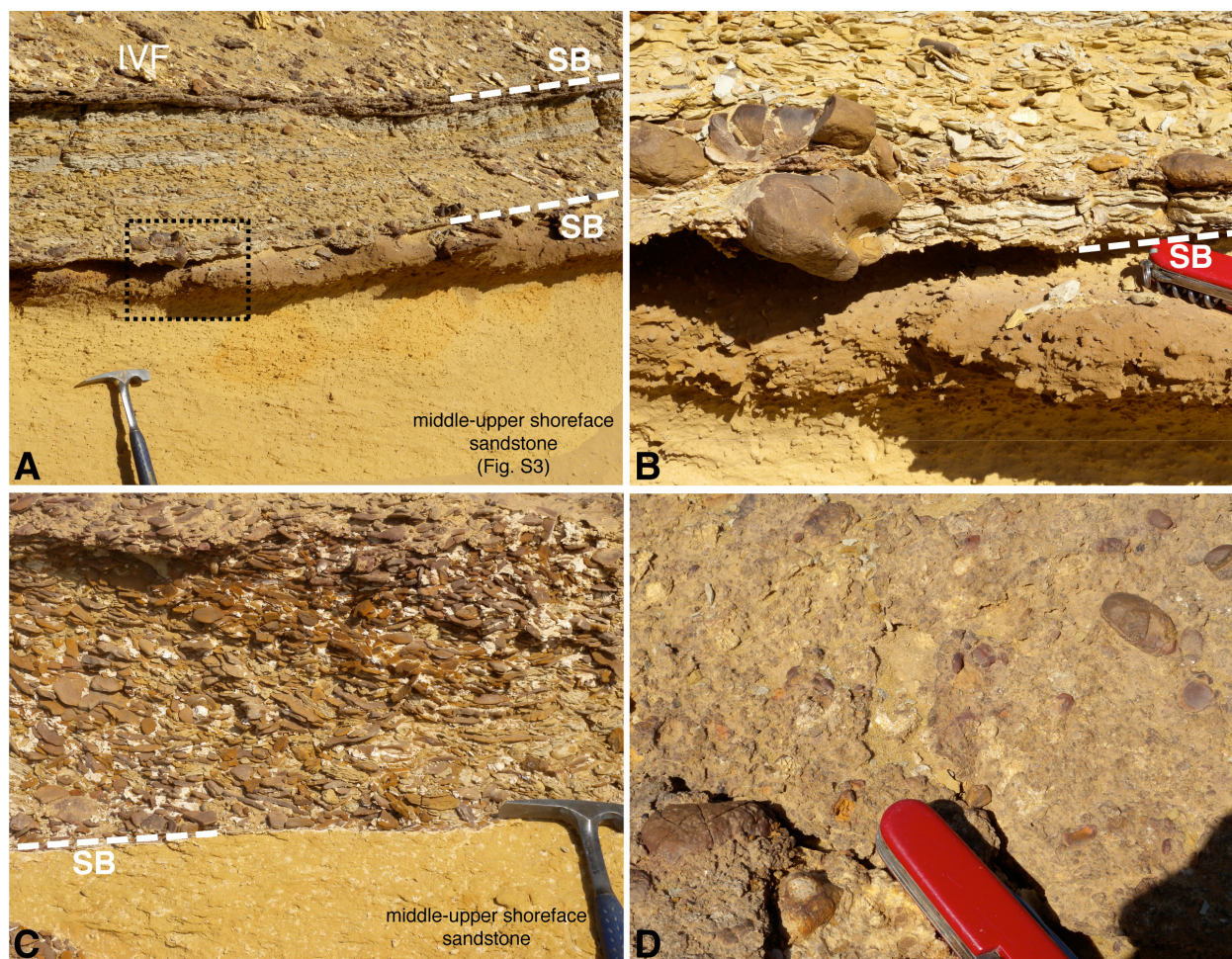


Figure DR4. Detail of sequence boundary (SB) that defines the base of the IVF. (A) SB marking the contact between very fine sandstone deposited in middle-upper shoreface environments (yellowish tan sandstone with hammer resting on it; Fig. DR2) and the IVF (greenish-tan mudstone with thin very fine sand interbeds above lower dashed line; see Fig. DR4). Two SBs, corresponding to at least two cycles of marine inundation and fluvial erosion, are labeled. The upper SB, which is a coarse ironstone pebble conglomerate, corresponds to one of the several internal SBs that occur within the main body of the IVF complex (Fig. DR8). Dashed box shows position of detail photo in B. (B) Close-up of main SB. Note cobble-sized, rounded ironstone clasts directly on the contact. These have been reworked and deposited as lags on the SB. (C) Main SB at base of IVF, with imbricated pebble conglomerate in sharp contact with underlying yellowish very fine sandstone of middle shoreface (Fig. DR2). This conglomerate was deposited in a fluvial environment and has yielded the eroded remains of whales and well-preserved remains of fully terrestrial mammals, including early elephants (Peters et al., 2009). (D) Bedding plane view of SB conglomerate, which consists of ironstone pebbles, eroded marine vertebrate teeth and bones, and terrestrial vertebrate remains.

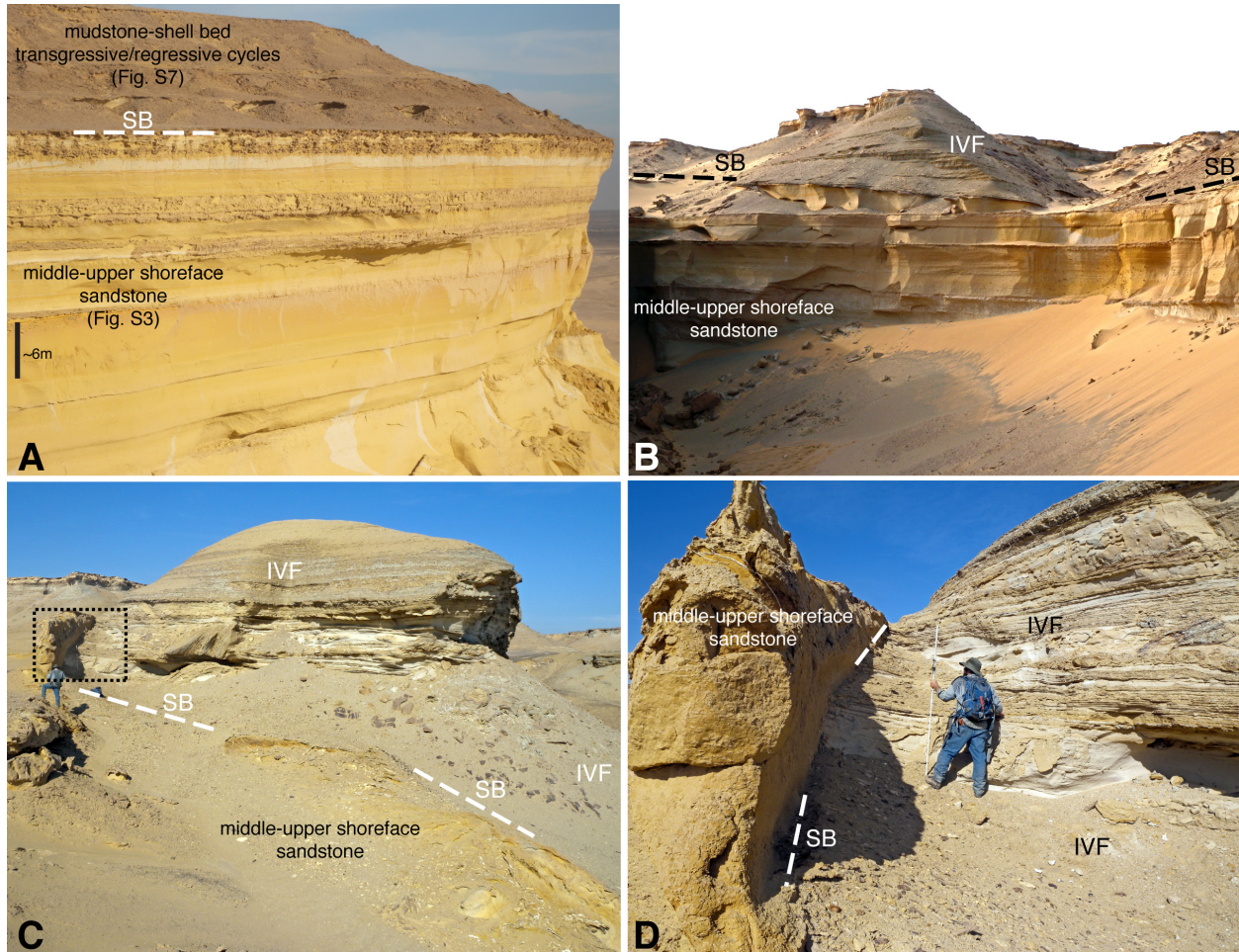


Figure DR5. Large-scale characteristics of the primary sequence boundary (SB) that defines the base of the IVF and the adjacent interfluvial. (A) Interfluvial south of the IVF complex. Here, the contact between the two sequences is close to the traditional boundary between the Birket Qarun and Qasr el-Sagha Formations. Couplets of shallow marine mudstone and sandy shell beds deposited during transgression are sharply juxtaposed on top of regressive marine sandstone. There is little obvious indication on the interfluvial that this stratigraphic boundary represents subaerial exposure of the region during sea level fall, but the excellent exposure at WH permits physical tracing into the IVF. (B) Lateral margin of the main body of the IVF. Note that horizontal beds of the underlying marine sequence are truncated by the SB. The slope on the IVF wall (SB) is ~ 4 degrees at this location. (C) Complex paleotopography at the base of the IVF. Here, the valley deepens and the IVF thickens considerably towards the right (north) in the image. Box shows area of detail in D. (D) Erosional remnant of burrowed marine sandstone deposited in middle shoreface laterally juxtaposed against fluvio-estuarine sediments of IVF. The vertical SB at this location was formed when rivers eroded and dissected the marine sandstones of the underlying sequence. Subsequent filling of the IVF during sea level rise buried this rarely-preserved erosional feature.

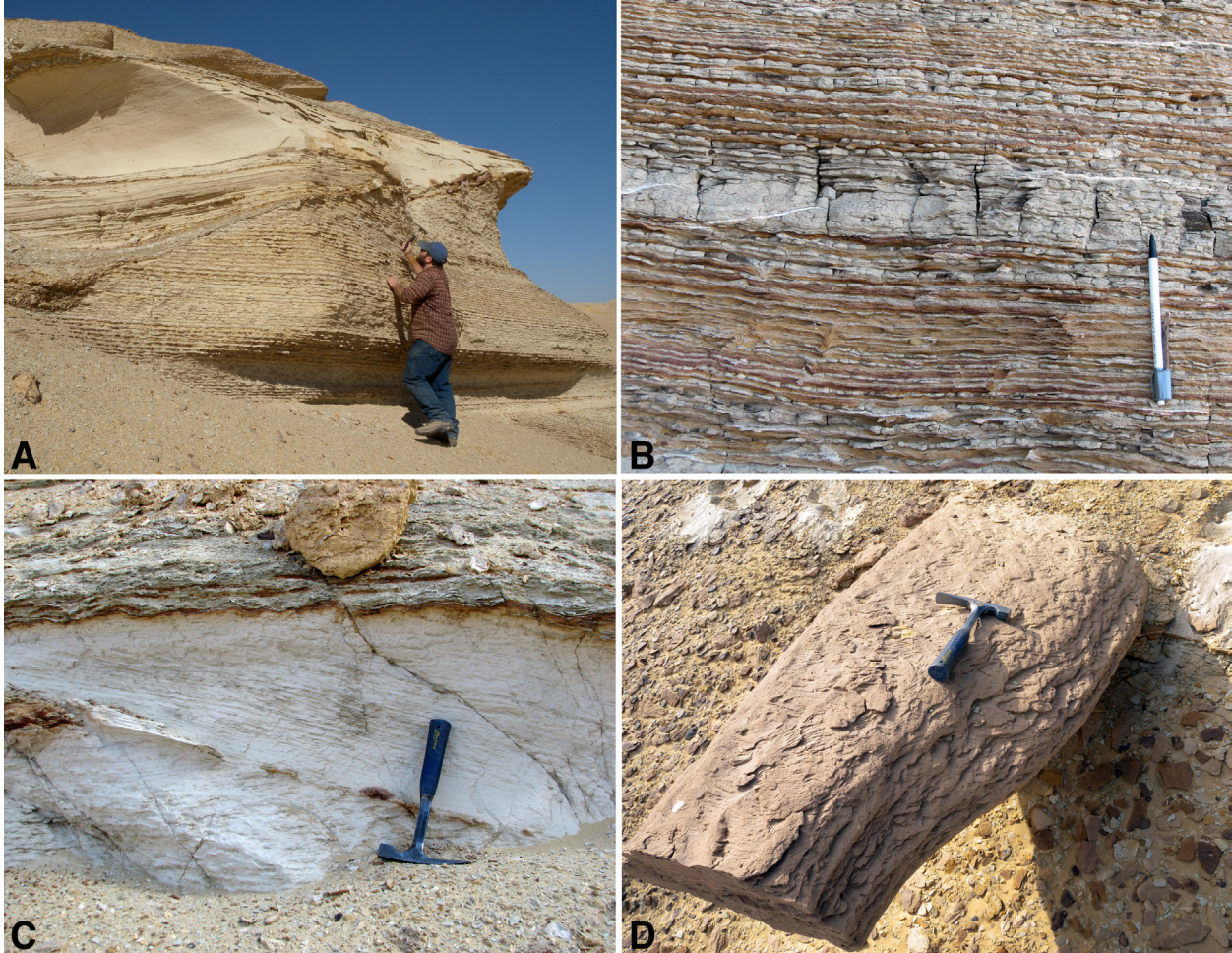


Figure DR6. Sedimentary features of the IVF. (A) Scour-and-fill (channel fill) structure truncating regularly bedded couplets of silty-mud and very fine sand. (B) Rhythmically bedded silty mud and sand, similar to the strata near the person in A. These mud-sand couplets, which lack marine fossils, are the dominant lithofacies throughout the entire thickness of the IVF. They are interpreted as tidal rhythmites deposited in fluvial-dominated estuaries and bay head deltas. (C) Tabular cross bedded, white, very fine sand with thin mud-partings defining laminations. Mud-sand couplets within such larger-scale bedforms are interpreted as tidal rhythmites. (D) Calcium carbonate-cemented concretion of sandstone with asymmetric current ripples within IVF. These lozenge-shaped concretions are abundant in the upper part of the IVF and their long axes are oriented preferentially in the direction of paleo-flow (note current ripples in D, which indicate a transport direction nearly parallel to long axis of concretion). These types of elongate concretions form during ground-water flow (Mozley and Matthew, 2005), which occurred during periods of base level fall, subaerial exposure of the IVF, and formation of subsidiary sequence boundaries (Fig. DR8).

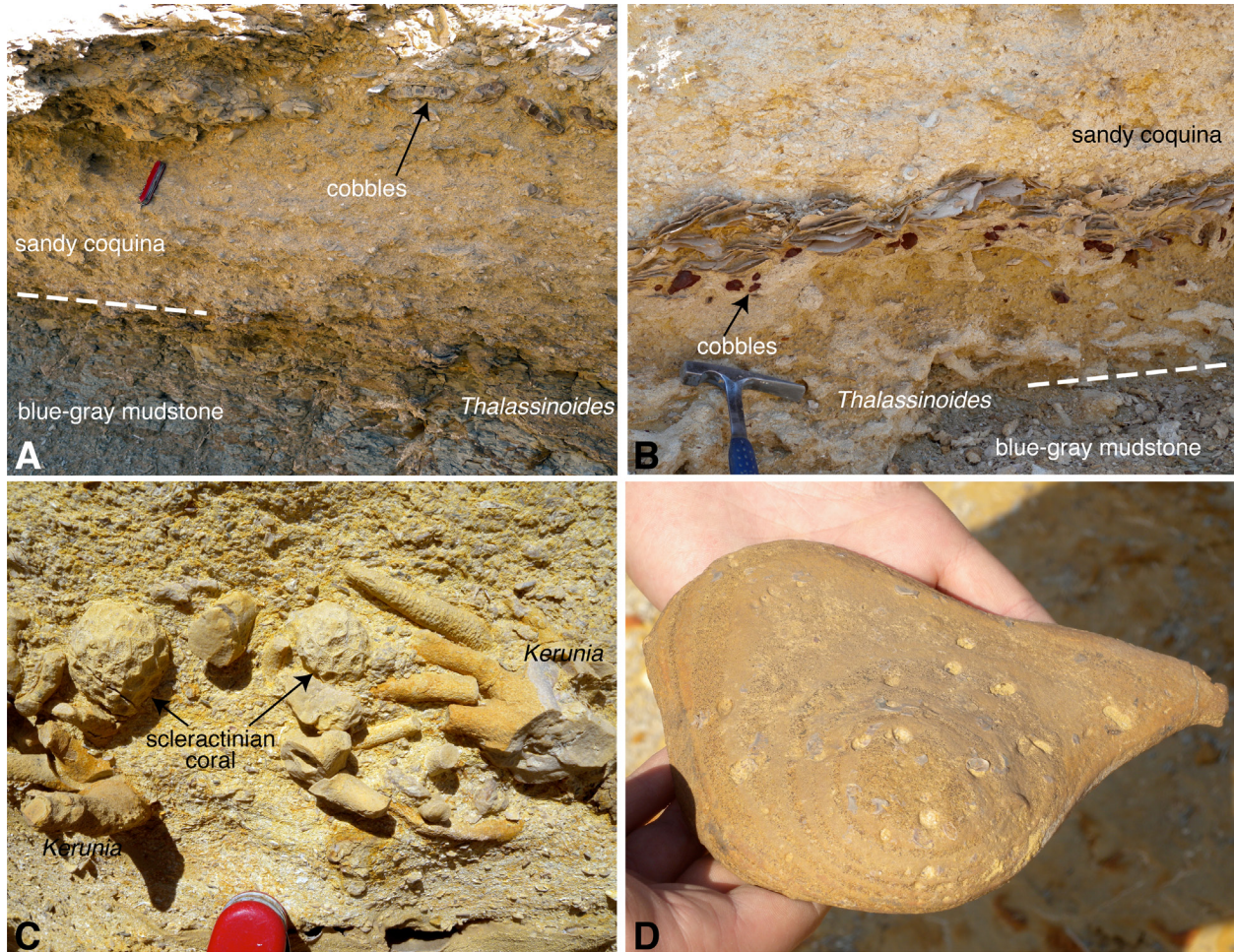


Figure DR7. Sedimentary and paleontological features of the marine ravinement surfaces (RS) that overlie the IVF. (A) Typical cycle boundary. Blue-gray mudstone with small bivalves and gastropods is abruptly overlain by a skeletal-rich, compound sandstone bed (shell bed). Large *Thalassinoides* burrows, filled with skeletal-rich sand, penetrate down into the mudstone up to 1 m, obscuring the contact. The skeletal beds have complex internal stratification and typically have scattered sandstone cobbles near their midsection. (B) Second example of RS cycle boundary. Note iron-oxide stained cobbles underlying a densely packed bed of well-preserved *Carolia* (anomiid bivalve). The cobbles derive from ironstone concretions that have been reworked from underlying sediments during transgression. (C) Coarse skeletal lag in an RS that caps the IVF. A diverse assemblage of scleractinian corals, echinoids, gastropods, bivalves, and the enigmatic cnidarian (?) *Kerunia* characterize the RS shellbeds overlying the IVF complex. These fossils indicate that normal marine shelf conditions were restored to the area by continuing sea level rise after formation of the IVF. (D) Cobble from an IVF-capping RS that has been weathered out of a shell bed. Note oyster attachment scars and *Trypanites* borings, indicating that the cobble was exposed and rounded on the sea floor.

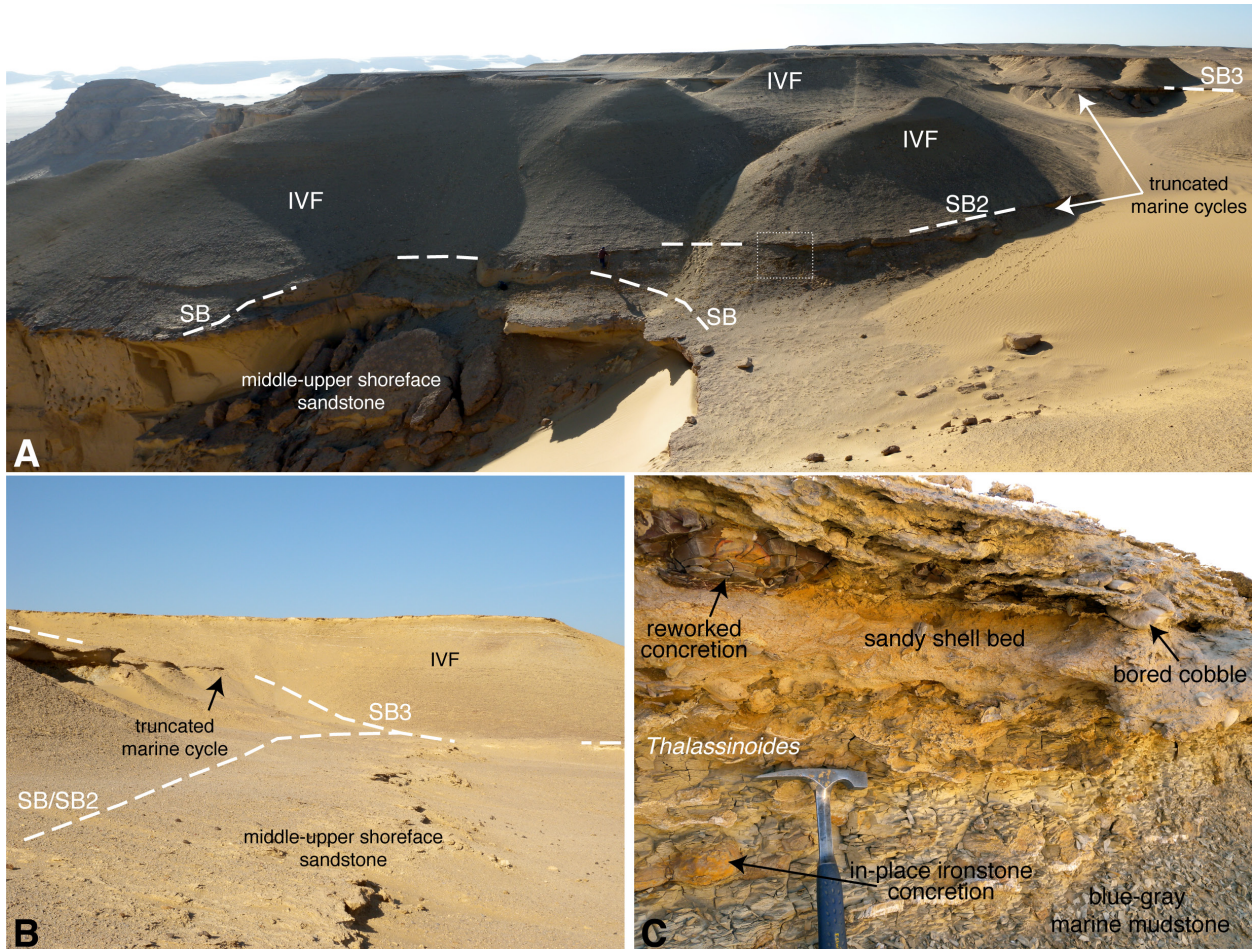


Figure DR8. Small-scale sequences preserved as erosional remnants along the southern margin of the IVF, near the intersection with the interfluvial. The large-scale geometries of the complex 3D geometries of the upper IVF are difficult to illustrate and therefore the key features are annotated on the photos. (A) Overview showing two subsidiary SBs (SB2-SB3) defined by marine cycles that are encased above, below and laterally within IVF sediments. Both of these marine cycles are completely truncated within 10-20 m of the main body of the IVF (towards viewer). Thin dashed box shows location of detail in C. (B) View of SB3 in A, but on other side of IVF ridge. Note the prominent marine ledge, which is identical to the marine cycles shown in Fig. DR7, is truncated by the IVF, which consists of fluvio-estuarine sediments like those illustrated in Fig. DR6. This particular marine cycle can be traced across the entire interfluvial (left in photo) but is truncated against the IVF, indicating that a period of marine inundation of the region was followed by erosion and additional IVF formation. (C) Detail of one of the marine cycles encased within the IVF (similar to cycles in Fig. DR7). The top of this cycle can be traced laterally into a SB conglomerate (in this case, the upper SB in Fig. DR4A) that clearly consists of material that was reworked and transported, including ironstone concretions that were eroded from the marine mud (Fig. DR 4B).

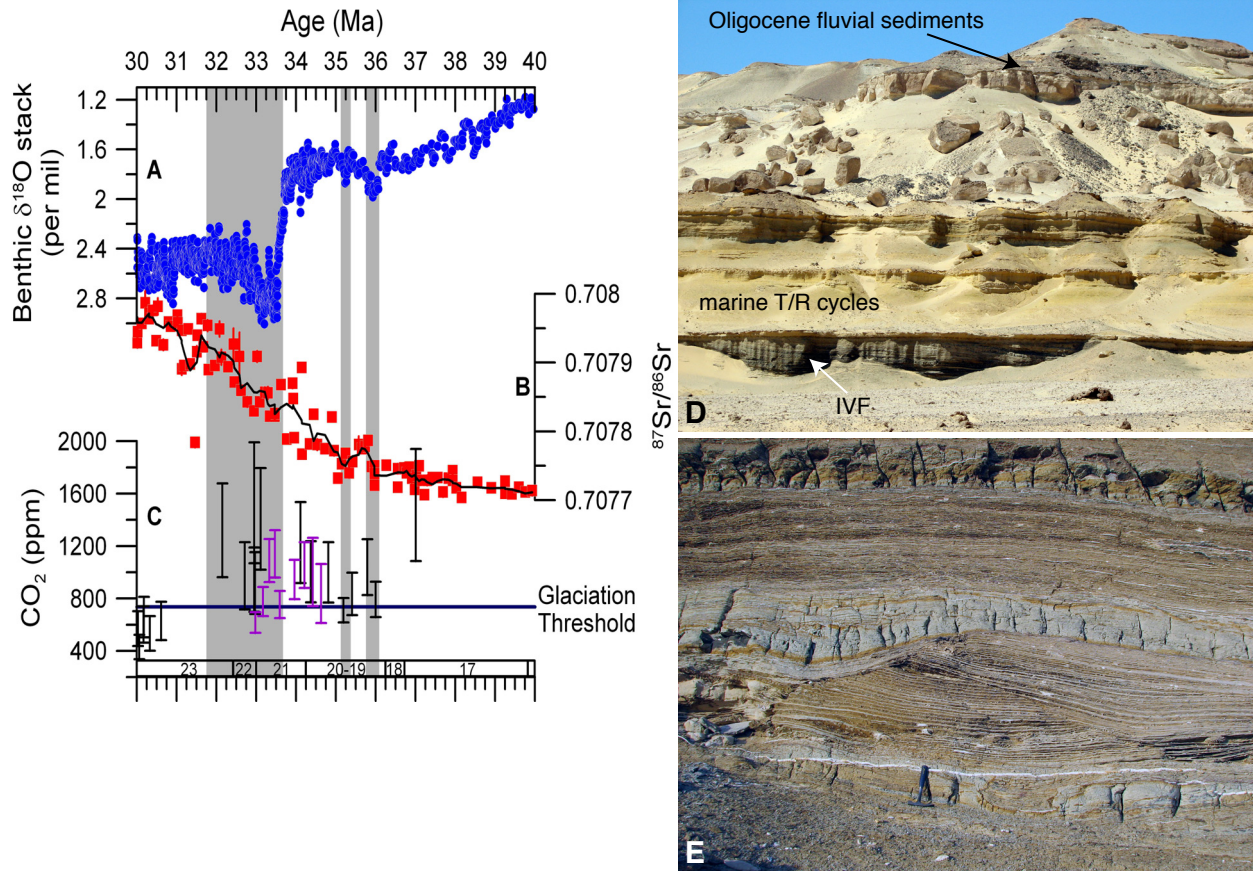


Figure DR9. Evidence for second episode of fluvial incision at WH ~ 35.1 Ma. (A-C) Oxygen, strontium, and CO_2 , records, as in Fig. 3 in the main body of the text. Note a second small increase in $\delta^{18}\text{O}$, continued increase in strontium isotopes, and a second decrease in CO_2 to below the hypothesized 750 ppm threshold for Antarctic Ice Sheet growth (highlighted by thin gray bar at ~ 35.1 Ma). (D) Top of Eocene section at WH, showing Oligocene fluvial sediments unconformably overlying Eocene marine sediments. Another IVF, located entirely within late Eocene marine sediments, occurs at the base of the outcrop. The second IVF is ~ 80 m above the IVF documented in the main body of the text (Fig. DR10). (E) Detail of upper, younger IVF at WH. This second, upper IVF succession at WH is lithologically and stratigraphically nearly identical to the lower IVF complex. We hypothesize that this second, younger episode of IVF formation at WH corresponds to the second transient drop in CO_2 illustrated in panel C. However, because this IVF has not yet been mapped or studied in great detail, we cannot estimate the minimum sea level fall with which it is associated. Its presence, however, does provide tangible support for the hypothesized threshold CO_2 response discussed here.

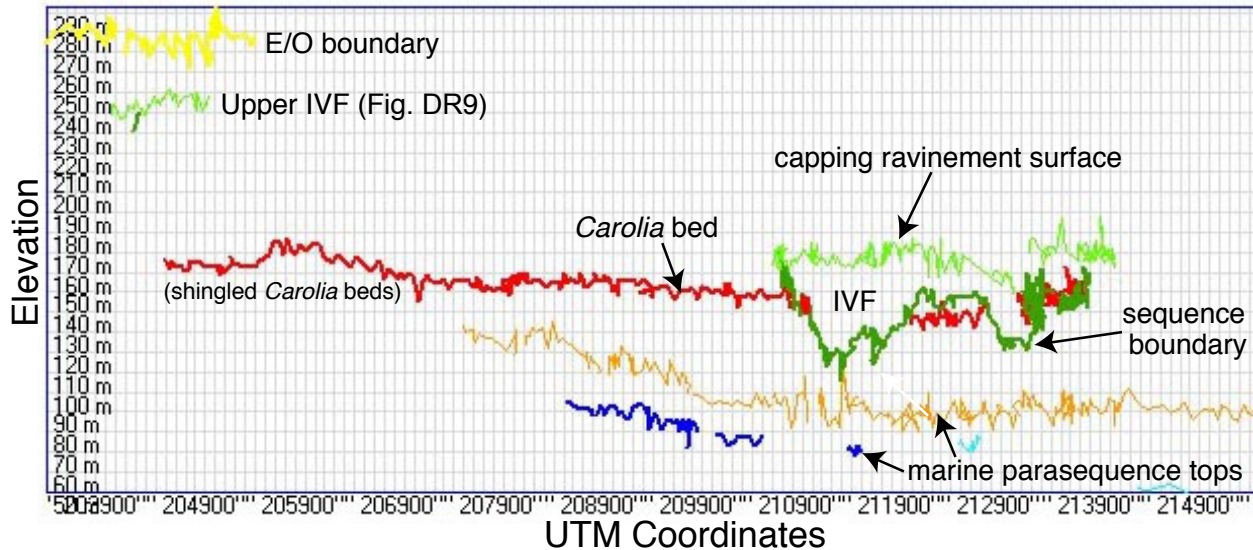


Figure DR10. Unprocessed GPS position data for physically traced stratigraphic surfaces at WH. Data have been projected onto a plane oriented parallel to the mean strike of aggregate bed traces (47.75° E of N). Much of the local, short wavelength variation in the line traces reflects standard vertical position error in GPS measurements whereas longer wavelength trends reflect actual variation in stratal geometry. For example, the trace of the sequence boundary that defines the IVF base (dark green) has significant vertical relief (basis for text Fig. 2), as do the marine parasequence tops beneath the IVF (gold and blue traces). Both reflect real depositional relief associated with the sequence boundary (Fig. 2) and progradational clinoformal geometry, respectively. Red trace is a prominent anomiid bivalve (*Carolia*) bed that forms the traditional base of the Qasr el-Sagha Formation. This distinct shell bed is clearly truncated by the IVF. The accuracy of the left portion of the red trace (labeled “shingled *Carolia* beds”) is, however, uncertain because the capping marine ravinement surface, which has abundant *Carolia*, impinges on the interfluvial at ~ 170 m elevation. This impingement causes shingling of shell beds from the two sequences that are difficult to distinguish. For this reason, it is likely that the red trace shifts to a non-equivalent *Carolia*-bearing bed near coordinate 206900. Gray grid lines represent 10 m in vertical dimension, 100 m in horizontal dimension.

Supplemental References

- Bamber, J.L., Riva, R.E.M., Vermeersen, B.L.A., and LeBrocq, A.M., 2009, Reassessment of the potential sea-level rise from a collapse of the West Antarctic ice sheet: *Science*, v. 324, 901-903.
- Cisne, J.L., 1986, Earthquakes recorded stratigraphically on carbonate platforms: *Nature*, v. 323, p. 320-322.
- Clark, P.U., Mitrovica, J.X., Milne, G.A., and Tamisiea, M.E., 2004, Sea-level fingerprinting as a direct test for the source of global meltwater pulse 1A: *Science*, v. 295, p. 2438-2441.
- Crittenden, M.D., 1960, Deformation of Bonneville shore lines. *GSA Bulletin*, v. 71, p. 1846.
- DeConto R.M. *et al.*, 2008, Thresholds for Cenozoic bipolar glaciation: *Nature*, v. 455, p. 652-656.
- Eldrett, J.S., Harding, I.C., Wilson, P.A., Butler, E., and Roberts, A.P., 2007, Continental ice in Greenland during the Eocene and Oligocene: *Nature*, v. 446, p. 176-179.
- Gradstein, F., Ogg, J., and Smith, A., 2004, *A geologic time scale*: Cambridge Univ. Press, Cambridge.
- Guiraud, R., and Bosworth, W., 1999, Phanerozoic geodynamic evolution of northeastern Africa and the northwestern Arabian platform: *Tectonophysics*, v. 315, p. 73-108.
- Hardenbol, J., Jacques, T., Martin, F.B., Pierre-Charles, G., and Vail, P.R., 1998, Mesozoic and Cenozoic sequence chronostratigraphy framework of European basins: *SEPM Special Publication 60*, p. 3-13.
- Kennett, J.P., and Stott, L.D., 1990, Proteus and proto-Oceanus: ancestral Paleogene oceans as revealed from Antarctic stable isotopic results, ODP Leg 113. *Proceedings of ODP, Science Results*, v. 113, p. 865-880.
- Larsen, H.C., Saunders, A.D., Clift, P.D., Beget, J., Wei, W., Spezzaferri, S., et al., 1994, Seven million years of glaciation in Greenland: *Science*, v. 264, p. 952-955.
- Lunt, D.J., Foster, G.L., Haywood, A.M., and Stone, E.J., 2008, Late Pliocene Greenland glaciation controlled by a decline in atmospheric CO₂ levels: *Nature*, v. 454, p. 1102-1105.
- MacEachern, J.A., Pemberton, S.G., Gingras, M.K., and Bann, K.L., 2007, *in* Miller, W. III, ed., *Trace fossils: concepts, problems, prospects*: Elsevier, Amsterdam, p. 52-77.

- Martini, E., 1971, *in* Farinacci, A., ed., Proceedings of the second planktonic conference, p. 739-785.
- Mead, G.A., and Hodell, D.A., 1995, Controls on the $^{87}\text{Sr}/^{86}\text{Sr}$ composition of seawater from the middle Eocene to Oligocene: Hole 689B, Maud Rise, Antarctica: *Paleoceanography*, v. 10, p. 327-346.
- Mitrovica, J.X., Gomez, N., and Clark, P.U., 2009, The sea-level fingerprint of West Antarctic collapse: *Science*, v. 323, p. 753.
- Moucha, R. *et al.*, 2008, Dynamic topography and long-term sea-level variations: there is no such thing as a stable continental platform: *EPSL*, v. 271, 101-108.
- Mozley, P.S., and Matthew, D.J., 2005, Internal structure and mode of growth of elongate calcite concretions: evidence for small-scale microbially induced chemical heterogeneity in groundwater: *GSA Bulletin*, v. 117, p. 1400-1412.
- Pagani, M., Zachos, J.C., Freeman, K.H., Tipple, B., and Bohaty, S., 2005, Marked decline in atmospheric carbon dioxide concentrations during the Paleogene: *Science* v. 309, p. 600-603.
- Perch-Nielsen, K., 1989, *in* Bolli, H. M., Saunders, J. B., and Perch-Nielsen, K., eds., *Plankton stratigraphy*: Cambridge Univ. Press, Cambridge, p. 427-554.
- Peters, S.E., Antar, M.S.M., Zalmout, I.S., and Gingerich, P.D., 2009, Sequence stratigraphic control on preservation of late Eocene whales and other vertebrates at Wadi Al-Hitan, Egypt: *Palaios*, v. 24, p. 290-302.
- Watts, A.B., 1982, Tectonic subsidence, flexure and global changes of sea level: *Nature*, v. 297, p. 469-474.
- Wellner, R.W., and Bartek, L.R., 2007, The effect of sea level, climate and shelf physiography on the development of incised-valley complexes: a modern example from the East China Sea: *Journal of Sedimentary Research*, v. 73, p. 926-940.
- Zachos, J., Pagani, M., Sloan, L., Thomas, E., and Billups, K., 2001, Trends, rhythms, and aberrations in global climate 65 Ma to present: *Science*, v. 292, p. 686-693.

Zachos, J.C., Dickens, G.R., and Zeebe, R.E. An early Cenozoic perspective on greenhouse gas warming and carbon-cycle dynamics: *Nature*, v. 451, p. 279-383.